

# A Kinematic Model for the Narrow-Line Region in NGC 4151<sup>1</sup>

D.M. Crenshaw<sup>2,3</sup>, S.B. Kraemer<sup>2</sup>, J.B. Hutchings<sup>4</sup>, L.D. Bradley II<sup>5</sup>, T.R. Gull<sup>6</sup>,  
M.E. Kaiser<sup>5</sup>, C.H. Nelson<sup>7</sup>, J.R. Ruiz<sup>2</sup>, & D. Weistrop<sup>7</sup>

Received \_\_\_\_\_; accepted \_\_\_\_\_

---

<sup>1</sup>Based on observations made with the NASA/ESA Hubble Space Telescope. STScI is operated by the Association of Universities for Research in Astronomy, Inc. under NASA contract NAS5-26555.

<sup>2</sup>Catholic University of America and Laboratory for Astronomy and Solar Physics, NASA's Goddard Space Flight Center, Code 681, Greenbelt, MD 20771

<sup>3</sup>crenshaw@buckeye.gsfc.nasa.gov

<sup>4</sup>Dominion Astrophysical Observatory, National Research Council of Canada, 5071 W. Saanich Rd., Victoria, B.C. V8X 4M6, Canada

<sup>5</sup>Department of Physics and Astronomy, Johns Hopkins University, Baltimore, MD 21218

<sup>6</sup>NASA's Goddard Space Flight Center, Laboratory for Astronomy and Solar Physics, Code 681, Greenbelt, MD 20771

<sup>7</sup>Department of Physics, University of Nevada, Las Vegas, 4505 Maryland Parkway, Las Vegas, NV 89154-4002

## ABSTRACT

We present a simple kinematic model for the narrow-line region (NLR) of the Seyfert 1 galaxy NGC 4151, based on our previous observations of extended [O III] emission with the Space Telescope Imaging Spectrograph (STIS). The model is similar to a biconical radial outflow model developed for the Seyfert 2 galaxy NGC 1068, except that the bicone axis is tilted much more into our line of sight ( $40^\circ$  out of the plane of the sky instead of  $5^\circ$ ), and the maximum space velocities are lower ( $750 \text{ km s}^{-1}$  instead of  $1300 \text{ km s}^{-1}$ ). We find evidence for radial acceleration of the emission-line knots to a distance of 160 pc, followed by deceleration that approaches the systemic velocity at a distance of 290 pc (for a distance to NGC 4151 of 13.3 Mpc). Other similarities to the kinematics of NGC 1068 are: 1) there are a number of high-velocity clouds that are not decelerated, suggesting that the medium responsible for the deceleration is patchy, and 2) the bicone in NGC 4151 is at least partially evacuated along its axis. Together, these two Seyfert galaxies provide strong evidence for radial outflow (e.g., due to radiation and/or wind pressure) and against gravitational motion or expansion away from the radio jets as the principal kinematic component in the NLR.

*Subject headings:* galaxies: individual (NGC 4151) – galaxies: Seyfert

## 1. Introduction

The study of the kinematics of the narrow line region (NLR) in Seyfert galaxies is important, because it has the potential to reveal the dynamical forces at work on the emission-line gas within about one kpc of the nucleus. In this region, the central supermassive black hole presumably dominates the kinematics, due to its gravitational influence and/or the radiation, winds, and jets that emanate from its immediate surroundings. With the Hubble Space Telescope (HST), we have the ability to resolve the emission-line knots within the NLR and with the two-dimensional detectors of the Space Telescope Imaging Spectrograph (STIS), we can measure their velocities accurately and efficiently. In this paper, we concentrate on STIS spectra of the apparently brightest Seyfert 1 galaxy, NGC 4151, and compare our results to those from a kinematic study based on STIS spectra of the brightest Seyfert 2 galaxy, NGC 1068 (Crenshaw & Kraemer 2000a, hereafter CK2000).

The NLR of NGC 4151 as defined by HST [O III] images (Evans et al. 1993) is biconical in shape with the apex located at the bright nucleus, and contains numerous bright emission-line knots and filaments. Evans et al. find a projected half-opening angle of  $37.5^\circ \pm 5^\circ$  for the bicone and a position angle (PA) of the bicone axis on the sky of  $60^\circ \pm 5^\circ$ . The extended narrow-line region (ENLR), at distances greater than  $6''$  from the nucleus, lies within the extrapolated bicone, but most of the emission from this region is concentrated between position angles  $30^\circ$  and  $60^\circ$  (Pérez-Fournon & Wilson 1990). Ground-based spectroscopy has revealed that the [O III] and H I velocity fields are very similar at these distances (Pedlar et al. 1992), indicating that the kinematics in the ENLR are dominated by galactic rotation.

Although the velocity field of the NLR in NGC 4151 (at distances less than  $6''$  from the nucleus) is difficult to determine from the ground, Schulz (1990) found evidence for

outflow along the cones, superimposed on galactic rotation. With observations primarily from HST’s Faint Object Camera (FOC), which has a limited ability to obtain long-slit spectra, Winge et al. (1997, 1999) claimed that the dominant kinematic component is rotation. STIS observations and detailed kinematic models are crucial for testing these claims. As part of a STIS Key Project carried out by members of the Instrument Definition Team, we have accumulated a number of observations of NGC 4151. Our previous results on these data are described in Hutchings et al. (1998, 1999), Kaiser et al. (2000), Nelson et al. (2000), and Kraemer et al. (2000). We describe the observations that are pertinent to our kinematic model in the next section.

We take the systemic velocity of NGC 4151 to be  $997 \text{ km s}^{-1}$ , based on H I observations of the outer regions of the host galaxy (Pedlar et al. 1992). For a Hubble constant of  $H_0 = 75 \text{ km s}^{-1} \text{ Mpc}^{-1}$  and a distance to NGC 4151 of 13.3 Mpc,  $0''.1$  corresponds to 6.4 pc.

## 2. Previous STIS Observations and Results

Our first STIS observation was a slitless spectrum of the  $H\beta$  and  $[\text{O III}]\lambda\lambda 4959, 5007$  emission at a spectral resolving power of  $\lambda/\Delta\lambda \approx 8000$  (Hutchings et al. 1998). By comparing the slitless spectrum with an archival WFPC2 image obtained through a narrow-band  $[\text{O III}]$  filter, we were able to determine the radial velocities and velocity dispersions of about 40 bright emission-line knots (with sizes on the order of  $0''.2$ ). We could also identify about 10 knots in a slitless spectrum of the C IV region, and found that their velocities were consistent with the  $[\text{O III}]$  measurements. We found that the highest velocities are close to the nucleus, and, in general, the emission-line knots are blueshifted to the southwest and redshifted to the northeast. A rotation curve cannot match the observed radial velocities as a function of distance. We proposed a simple model consistent with the geometry of Evans et al. (1993) to explain the gross kinematics: radial outflow along the

surface of a bicone, with an opening angle of  $80^\circ$  and a line of sight that is  $10^\circ$  outside of the cones.

In Kaiser et al. (2000), we presented slitless spectra of several spectral regions at a more favorable roll angle than that of the Hutchings et al. (1998) observations. Using these data, we were able to determine radial velocities for a number of additional emission-line knots. In Figure 1, we compare the radial velocities for the emission-line knots in common in these two studies. The average difference in radial velocity is only  $47 \text{ km s}^{-1}$ , which indicates the reliability of this observational technique. In Kaiser et al. (2000), an attempt to fit the radial velocities as a function of distance with a rotating disk model and point-source mass was not satisfactory; the transition between blueshifted and redshifted velocities is much steeper than observed, and an unreasonably large central mass is required:  $10^{10} M_\odot$  if all clouds are included, and  $4 \times 10^8 M_\odot$  if clouds with radial velocities of only  $200 \text{ km s}^{-1}$  or less are included. Thus, we found that outflow is extremely likely, since gravitational motions (including infall) cannot account for the high velocities. There is no strong correlation between velocity or velocity dispersion and the positions of the radio knots, which indicates that jet acceleration is not important; wind or radiation pressure are more likely sources of the acceleration.

In Hutchings et al. (1999), we used narrow-band WFPC2 images of NGC 4151 to isolate faint line emission at high velocities for several ions. Radial velocities up to  $1400 \text{ km s}^{-1}$  were seen in both approach and recession on both sides of the nucleus, indicating a separate kinematic component from that seen in the bright emission-line knots. We will not attempt to model this component in the current paper; additional progress on this component is likely to come from planned long-slit observations at high spectral resolution.

In Nelson et al. (2000), we presented long-slit ( $52'' \times 0''.1$ ) spectra of NGC 4151, obtained at low spectral resolving power ( $\lambda/\Delta\lambda \approx 1000$ ) over the  $1150 - 10,000 \text{ \AA}$  range

at two position angles:  $221^\circ$  (passing through the nucleus) and  $70^\circ$  (passing  $0''.1$  south of the nucleus, see Figure 1 in Nelson et al. 2000 for the slit placements superposed on WFPC2 [O III] images). Although these data do not have the spatial coverage and spectral resolution of the slitless spectra, the slit allowed us to determine the location and radial velocities of much weaker emission, including that between the bright emission-line knots. To determine the radial velocities, we used the [O III]  $\lambda 5007$  emission in  $0''.2$  bins along the  $0''.1$ -wide slit. We explored two basic models in this paper: radial outflow away from the nucleus and expansion away from the radio jet axis. We concluded that radial outflow provides the best match with the data.

### 3. Data Analysis and Measurements

We rely on our previous observations to develop a detailed kinematic model for the NLR of NGC 4151 in this paper. For our analysis of the slitless spectra, we use the measurements of Kaiser et al. (2000), which we have shown are consistent with those of Hutchings et al. (1998). For the long-slit spectra, we remeasured the [O III]  $\lambda 5007$  emission along the slit at each pixel location ( $0''.05$  intervals), rather than in  $0''.2$  bins, to avoid smoothing of features in the radial velocity curves. At some locations close to the nucleus, there are two distinct components of the [O III] emission at this spectral resolution. We fit the spectrum at each location with a local continuum plus a Gaussian for each clearly identifiable peak of [O III] emission, resulting in one or two kinematic components. We determined uncertainties in the radial velocities of the components from the errors in the Gaussian fits and from different reasonable continuum placements.

Figures 2 and 3 give the radial velocities, widths (full-width at half-maximum, corrected for the instrumental value of  $300 \text{ km s}^{-1}$ ), and fluxes as a function of angular distance from the nucleus for the long-slit spectra at the two position angles; our convention is that

negative positions represent the southwest direction. The radial velocity curves in the top plots are very similar to those determined by Nelson et al. (2000), except they show a little more structure due to the finer sampling. At distances less than  $4''$ , the emission-line knots southwest of the nucleus are blueshifted and the knots northeast of the nucleus are redshifted. At greater distances, the radial velocities approach the rotational velocities seen in the ENLR. High radial velocities (greater than  $\sim 300 \text{ km s}^{-1}$ ) tend to occur within  $\sim 1''$  of the nucleus, although low radial velocities occur in this region as well. In many cases, the structure in the radial velocity curves can be attributed to the varying contributions of emission-line knots and background emission to the total [O III] emission as a function of position. The knotty structure can be seen in the bottom plots of Figures 2 and 3. The middle plots in Figures 2 and 3 show that there are no strong trends in the velocity widths, except that the lower velocity clouds at large distances tend to have smaller widths. The velocity widths are due to superposition of emission knots with distinct velocities as well as internal dispersion within each knot.

In Figure 4, we compare the radial velocities derived from the long-slit spectra with those from the slitless spectra; the number of points are limited, since there only a few bright emission-line knots that lie along the slit locations. Again, the measured radial velocities are very similar, with no evidence for systematic offsets as a function of velocity or dispersion. The average difference in radial velocity is only  $37 \text{ km s}^{-1}$ . We conclude that the two observational techniques provide reliable radial velocities; slitless spectra at moderate resolution are useful for obtaining velocities of all of the bright emission-line knots in a single observation, whereas long-slit low-resolution spectra are helpful for determining the kinematics of all of the emission along a particular direction.

#### 4. A Biconical Outflow Model

Our model for NGC 4151 is based on a previous kinematic model for the NLR in the Seyfert 2 galaxy NGC 1068 (CK2000). From STIS low-resolution long-slit spectra of the [O III] emission, we found that a simple model of biconical radial outflow provides a good match to the radial velocities as a function of distance from the hot spot in NGC 1068. In that model, the bicone is evacuated along its axis, which is inclined only  $5^\circ$  out of the plane of the sky. The emission-line knots show radial acceleration to a distance of  $\sim 140$  pc from the hot spot, followed by deceleration that approaches the systemic velocity at  $\sim 310$  pc. The deceleration is likely due to collision with a patchy and anisotropically distributed ambient medium.

For the biconical model of NGC 4151, we assume that the two cones have identical properties (geometry, velocity law, etc.), a filling factor of one within the defined geometry, and no absorption of [O III] photons. The parameters that are allowed to vary in our code are the extent of each cone along its axis ( $z_{max}$ ), its minimum and maximum half-opening angles ( $\theta_{inner}$  and  $\theta_{outer}$ ), the inclination of its axis out of the plane of the sky ( $i_{axis}$ ), and the velocity law as a function of distance from the nucleus. Our code generates a two-dimensional velocity map and samples this map with a slit that matches the position, orientation, and width of the observational slits. Note that we are only attempting to match the observed radial velocities with the model, and not the observed line widths or fluxes.

Given the success of our model for NGC 1068, we assumed the same velocity law for NGC 4151: constant acceleration to a maximum velocity ( $v_{max}$ ) at a turnover radius ( $r_t$ ), followed by a constant deceleration to zero velocity at the greatest extent of the cone ( $= z_{max}/\cos \theta_{outer}$ ). Then we adjusted the other parameters of the model to determine if a reasonable match to the observed radial velocities could be obtained. First, we tilted the bicone axis out of the sky until the observed form of the model radial velocity curves

matched that of the observations. For NGC 4151, this occurs when the bicone moves completely out of the plane of the sky, so that one cone is blueshifted and the other side is redshifted. Then, we varied the other parameters until we obtained a reasonable match with the observations. Since the observed radial velocity curves show significant scatter, we did not attempt to fine-tune the models; instead we settled for an illustrative model that matches the overall trends.

The parameters for our kinematic model of NGC 4151 are shown in Table 1; values for the model of NGC 1068 are given for comparison. The bicone opening angles, maximum extent, and turnover radius are very similar for the two models. The maximum velocity at the turnover is much lower in NGC 4151, which may be due to its lower intrinsic luminosity (see the Discussion). The principal difference between the two models is the viewing angle, with the bicone axis of NGC 4151 much closer to the line of sight. However, as we note in the Discussion, the inclination is not enough to place the line of sight into the ionization cone. Given the inclination angle, we find that the *projected* maximum half-opening angle onto the plane of the sky is  $43.5^\circ$ , which is close to the  $37.5^\circ \pm 5^\circ$  determined from the HST images by Evans et al. (1993).

Two-dimensional velocity maps for the model of NGC 4151 are given in Figure 5, along with the slit positions and widths that correspond to our long-slit observations. For demonstration, we show only the front and back sides of the outermost surface (at  $\theta_{outer}$ ). For comparison, we show the same surfaces in Figure 6 for our model of NGC 1068 (not shown in CK2000 due to space limitations). In both figures, the models are aligned so that the projected bicone axis on the sky is vertical, and northeast is at the top. The inclination of the bicone axis is NGC 4151 is such that the entire northeast cone is redshifted, and the entire southwest cone is blueshifted. By contrast, the axis for NGC 1068 is inclined by only  $5^\circ$  so that blueshifts and redshifts of similar magnitude occur in both cones (see

CK2000 for more details). The effects of our acceleration plus deceleration velocity laws, modified by projection of the velocity vectors from the bicone, are visible in these images. One interesting feature of the NGC 4151 model is that the maximum radial velocities occur very close to the nucleus on the plane of the sky, regardless of slit position.

## 5. Comparison of the Observations and Models

First, we compare the models with the long-slit observations. Figure 7 shows the envelopes of radial velocities from the model of NGC 4151, extracted from the two slit positions, compared to the observed radial velocities (relative to systemic). There are four distinct components of the envelope in each plot, corresponding to the four quadrants of the bicone intersected by the slit. The width of the envelope is determined by the range in half-opening angle, and the relative amplitudes are determined by the inclination of the bicone axis. Although the match is not perfect, the overall trends are reproduced. The major discrepancy is that this model does not explain the blueshifted velocities in the  $-150$  to  $-300$   $\text{km s}^{-1}$  range (relative to systemic) in the southwest cone. This discrepancy could be eliminated by filling in the southwest cone with emitting material, which would fill in the gap in the plots, but would also fill in regions that are not occupied by observed points. Thus, the bicone for the most part must be evacuated along its axis. Our model also does not explain the emission knots with very high velocities ( $> 700$   $\text{km s}^{-1}$  relative to systemic), which is also the case for NGC 1068. As noted in CK2000, this indicates that some emission-line knots do not experience a significant deceleration.

Next, we compare the models with the slitless observations. In the top plot of Figure 8, we show the slitless radial velocities as a function of position, relative to the nucleus at the origin. The magnitude of the radial velocity is represented by the size of the symbol, with “+” representing blueshift and “x” representing redshift, relative to the systemic velocity.

The plot is oriented such that the bicone axis, at  $PA = 60^\circ$ , is vertical. The trends discussed earlier can be seen in this plot (for a color-coded velocity map, see Hutchings et al. 1998).

The bottom plot in Figure 8 shows the observed radial velocities minus the model values. At each observed point, we have two model values to choose from: the average radial velocity for the front side and the average value for the back side; we adopt the value closest to the observed radial velocity and subtract. Although our kinematic model was calculated to fit the long-slit data, the small residual velocities in this plot show that it provides a reasonable fit to the slitless data as well. There is a mixture of positive and negative residuals in each cone, indicating the overall agreement between the model and observations. The two largest residuals in this plot identify the “rogue” blueshifted knots that apparently do not experience any deceleration, which correspond to knots 23 and 26 in Hutchings et al. (1998) and Kaiser et al. (2000).

In Figure 9 we plot the observed radial velocities vs. the model values at each point to show the magnitude of the residuals. Except for a few points, notably the two highly blueshifted knots, the residuals are relatively small and evenly distributed around the unity line. We conclude that our kinematic model provides a good match to the general trends seen in all of our slitless and long-slit data sets.

## 6. Discussion

The details of our kinematic model of NGC 4151 were inspired by STIS observations and a kinematic model of the NLR in NGC 1068. Since the outflow axis is nearly in the plane of the sky in NGC 1068, the trend of increasing velocity with distance to a turnover radius, followed by decreasing velocity, can be easily seen in this object, and the lack of emission along the cone axis in NGC 1068 is also clear (CK2000). The detailed kinematics of

the NLR in NGC 4151 have been more difficult to interpret, since it turns out that the cone axis is significantly out of the plane of the sky, and velocities from different radial distances are projected along the same line of sight (see Figure 5). However, by adopting the basic geometry and velocity law used for NGC 1068, we are able to construct a kinematic model of the NLR in NGC 4151 that matches the observed trends in radial velocity as a function of position. The only major changes were to reduce the maximum radial velocity from 1300 to 750 km s<sup>-1</sup>, and to tilt the bicone axis from 5° to 40° out of the plane of the sky. Thus, we have a basic model that can explain the NLR kinematics in both Seyfert galaxies.

### 6.1. Comparison with Other Models

Winge et al. (1997, 1999) claim that the dominant kinematic component in the NLR of NGC 4151 is rotation. However, there are several problems with this model. First, as we discussed earlier, the observed transition between blueshifted and redshifted radial velocities is much shallower than the predicted values from a Keplerian disk with a point-source mass. Thus, in addition to a point-source mass of  $5 \times 10^7 M_{\odot}$ , these authors must include an extended mass of order  $10^9 M_{\odot}$  in the inner  $0''.1$ , to match the shallow transition between blueshifted and redshifted velocities. To date, there is no confirmatory evidence for such an extended mass. Second, Winge et al. (1999) are only able to fit their low-velocity component (within 300 km s<sup>-1</sup> of systemic) with this model; the higher velocities require another explanation. Finally, we note that a rotation model cannot explain the kinematics of the NLR in NGC 1068, which shows blueshifts and redshifts of similar magnitude on both sides of the nucleus.

To explore the uniqueness of our model for NGC 4151, we have experimented with a number of different velocity laws and inclination angles, but with the same biconical geometry. We summarize our findings as follows. 1) Simple radial outflow at constant

velocity or acceleration cannot explain the decreasing velocities at distances  $> 1''$ .

2) Gravitational infall cannot produce the small radial velocities seen within  $1''$  of the nucleus. Also, as we pointed out in Kaiser et al. (2000), gravitational infall models require unreasonably high masses (on the order of  $10^{10} M_{\odot}$ ) to produce the high velocities that are seen. 3) Axon et al. (1998) propose a model for NGC 1068 in which the gas expands away from the radio jet (which is nearly coincident with the ionization cone axis). The simplest version of this model is one in which the velocity vectors are perpendicular to the bicone axis. As demonstrated by Nelson et al. (2000), this model cannot work for NGC 4151. As the bicone axis is tilted out of the plane of the sky, the velocity vectors in each of the two cones decrease in magnitude by the same amount, and there is no inclination angle that will yield the observed blueshifts on one side of the nucleus and redshifts on the other. 4) Nelson et al. (2000) show that a reasonably good match to the STIS observations can be obtained by assuming radial outflow, with velocity decreasing with distance as  $r^{-1/2}$ . We verify that this velocity law provides an acceptable solution for NGC 4151, except that there is some indication of acceleration of the clouds away from the nucleus at small distances (see Figure 7). We note that this velocity law does not work for NGC 1068, which shows clear acceleration of the clouds to an angular distance of  $\sim 1.7''$  (CK2000). Thus, our proposed model provides the best explanation at present for both Seyfert galaxies.

## 6.2. Geometry of the Bicone and Host Galaxy

The host galaxy of NGC 4151 is nearly face-on (inclination from our line of sight =  $20^{\circ}$ , PA of the major axis =  $22^{\circ}$ , see Pedlar et al. 1992). Given the inclination and PA of our kinematic model of the NLR, the bicone axis is inclined by  $\sim 40^{\circ}$  with respect to the host galaxy, and one side of each cone (corresponding to a low radial velocity quadrant in Figure 7) lies close to the galactic plane (similar to the case for NGC 1068, see CK2000). Thus,

our proposed geometry allows the gas in the galactic disk to be ionized by the continuum source and is compatible with the idea that this gas is the ENLR. The general agreement between ground-based [O III] and H I radial velocities at a distance of 10 – 20'' from the nucleus provides strong evidence for this idea (Pedlar et al. 1992); in particular, these observations indicate normal galactic rotation, with typical radial velocities of  $-70 \text{ km s}^{-1}$  in the southwest and  $+70 \text{ km s}^{-1}$  in the northeast. Our slitless observations are consistent with these values; they indicate an average radial velocity of  $-50 \pm 15 \text{ km s}^{-1}$  relative to systemic for the [O III] emission 10 – 20'' southwest of the nucleus (after correcting for an offset of  $-40 \text{ km s}^{-1}$  for the [O III] emission at the nucleus, relative to the systemic, see Kaiser et al. 2000). Thus, our observations confirm that the NLR and ENLR are two physically distinct regions in NGC 4151; from the kinematics, it appears that the transition from one region to the other occurs in the region 6'' to 10'' from the nucleus.

The standard unified model for Seyfert galaxies posits a thick molecular torus that produces ionization cones with sharp edges (Antonucci 1993). In this scheme, our line of sight to a Seyfert 1 galaxy should be inside the ionization bicone. However, the sum of the inclination and maximum half-opening angles from our model of NGC 4151 is  $76^\circ$  which places our line of sight  $14^\circ$  outside of the bicone. This discrepancy was pointed out Evans et al. (1993), who arrive at a viewing angle that is  $\sim 30^\circ$  outside of the bicone, based on the observed morphologies of the NLR and ENLR. Thus, NGC 4151 does not appear to fit the standard unified model. However, if the obscuring torus is not optically thick at all polar angles (cf., Evans et al. 1993; Konigl and Kartje 1994), then the ionization cones would have “fuzzy” edges, and NGC 4151 would offer no problems for this type of model.

### 6.3. Implications for Dynamical Models

Based on our observations and kinematic models, we find strong evidence for radial outflow in the NLRs of NGC 4151 and NGC 1068. The velocity flow is well-organized, suggesting that the emission-line clouds originate close to the nucleus and are forced outward from there. A linear increase in velocity with distance to a turnover radius provides a reasonable fit to the observations. There are two plausible interpretations of this trend. One is that the clouds in these two NLRs originated from an explosive outburst that occurred  $\sim 10^5$  years ago (the crossing time to a distance of  $\sim 150$  pc), which would naturally lead to a linear increase of velocity with distance. If this model is generally correct, then the NLRs in some Seyfert galaxies should be evacuated near the nucleus; so far there is no evidence for this in HST [O III] images (cf., Schmitt & Kinney 1996).

Another interpretation assumes a steady-state model, in which clouds are continuously ejected from the nucleus and experience approximately constant acceleration out to the turnover radius. Under this interpretation, the most likely sources of acceleration would be radiation and/or wind pressure. Radiative driving of resonance lines is an attractive means of accelerating the clouds, since a strong radiation field is obviously present. However, there is also evidence for outflowing winds in the form of highly ionized gas seen in absorption in the UV (Crenshaw et al. 1999) and X-rays (Reynolds 1997; George et al. 1998). Since the turnover radius is similar for the two Seyfert galaxies, the lower maximum velocity in NGC 4151 indicates a smaller acceleration. If the acceleration mechanism is radiation pressure, the lower maximum velocity in NGC 4151 may be due to a much lower luminosity, which is  $\sim 10\%$  of the intrinsic luminosity of NGC 1068 (Pier et al. 1994). In any event, future dynamical models will have to explain the roughly constant acceleration of the NLR clouds to the turnover point.

It is unlikely that the radio jets are responsible for the radial acceleration of the

emission line knots, since there is no apparent correlation of their radial velocities with radio knot location in either NGC 4151 (Kaiser et al. 2000) or NGC 1068 (CK2000). However, the radio jets may be responsible for evacuating the bicones along their axes, since the emission-line knots appear to be avoiding the radio knots in the inner NLRs of these two Seyferts (Kaiser et al. 2000; Capetti et al. 1997).

An unexpected result of this study and that of CK2000 is that the NLR clouds in NGC 4151 and NGC 1068 undergo deceleration at a distance of  $\sim 150$  pc from the nucleus. The deceleration cannot be due to gravity because an unreasonably high mass ( $\sim 10^{10} M_{\odot}$ ) is required at the distances and velocities of the turnover point. Following CK2000, the simplest explanation for the deceleration is that the clouds experience a drag force due to a surrounding ambient medium extending outward from the turnover point. In this interpretation, the emission knots with unusually high velocities have not experienced drag forces because they have passed through holes in the surrounding medium. Additional evidence for collision of the NLR clouds with an ambient medium comes from a study of the physical conditions in the NLR of NGC 1068 (Kraemer & Crenshaw 2000). Near the location of the velocity turnover in the blueshifted region of the northeast cone, we find evidence for an additional source of EUV ionizing radiation that is likely to be generated from the shock front as the clouds encounter the ambient medium. However, we note that these effects have not (as yet) been detected at other turnover points in NGC 1068 or in NGC 4151. Another clue to the ambient medium can be found from observations of the extended continuum in NGC 1068 (Crenshaw & Kraemer 2000b), which show very enhanced regions of electron-scattered continua. As pointed out by Kraemer & Crenshaw (2000), these are likely to be regions of highly-ionized, low-density (ionization parameter  $\approx 1$ , electron density  $\approx 100 \text{ cm}^{-3}$ ) gas which must nearly fill the bicone at these distances, and are therefore likely candidates for the decelerating media. Unfortunately, the glare from the nucleus of NGC 4151 prevents us from searching for a scattered continuum component

in its NLR.

## 7. Conclusions

The principal advantage of a kinematic model that invokes radial outflow in the NLR is that it can explain the observed radial velocities in both a Seyfert 1 galaxy (NGC 4151) and a Seyfert 2 galaxy (NGC 1068). Assuming that radial outflow is common in the NLR of all Seyfert galaxies, it is interesting (but not surprising) that the kinematic signature of circumnuclear gas within  $\sim 500$  pc of an active nucleus is probably different from that surrounding “inactive” supermassive black holes in nearby galaxies, in which gravitational motions dominate (e.g., M84, Bower et al. 1998). This may indicate that once a supermassive black hole “turns on” (e.g., due to an onset of fueling), radiation and/or wind pressure from the active nucleus will dominate the kinematics of the NLR.

It is intriguing that very similar geometries and velocity laws can explain the observed radial velocities in the two Seyfert galaxies that we have studied. This may indicate a common dynamical situation in all Seyferts, or it may just be a coincidence. New STIS observations of more Seyfert galaxies will be helpful in testing the general applicability of these kinematic models and providing the refinements needed for detailed dynamical models.

This work was supported by NASA Guaranteed Time Observer funding to the STIS Science Team under NASA grant NAG 5-4103.

## REFERENCES

- Antonucci, R. 1993, *ARA&A*, 31, 473
- Axon, D.J., Marconi, A., Capetti, a., Macchetto, F.D., Shreier, E., & Robinson, A. 1998, *ApJ*, 496, L75
- Bower, G.A., et al. 1998, *ApJ*, 492, L111
- Capetti, A., Macchetto, F.D., & Latannzi, M.G. 1997, *ApJ*, 476, 67
- Crenshaw, D.M. & Kraemer, S.B. 2000a, *ApJ*, 532, L101 (CK2000)
- Crenshaw, D.M. & Kraemer, S.B. 2000b, *ApJ*, 532, 247
- Crenshaw, D.M., Kraemer, S.B., Boggess, A., Maran, S.P., Mushotzky, R.F., & Wu, C.-C. 1999, *ApJ*, 516, 750
- Evans, I.N., Tsvetanov, Z., Kriss, G.A., Ford, H.C., Caganoff, S., & Koratkar, A.P. 1993, *ApJ*, 417, 82
- George, I.M., et al. 1998, *ApJS*, 114, 73
- Hutchings, J.B., Crenshaw, D.M., Kaiser, M.E., Kraemer, S.B., Weistrop, D., Baum, S., Bowers, C.W., Feinberg, L.D., Green, R.F., Gull, T.R., Hartig, G.F., Hill, G., and Lindler, D.J. 1998, *ApJ*, 492, L115.
- Hutchings, J.B., Crenshaw, D.M., Danks, A.C., Gull, T.R., Kraemer, S.B., Nelson, C. H., Weistrop, D., Kaiser, M.E., & Joseph, C.L. 1999, *AJ*, 118, 2101
- Kaiser, M.E., Bradley, L.D., II., Hutchings, J.B., Crenshaw, D.M., Gull, T.R., Kraemer, S.B., Nelson, C.H., Ruiz, J., & Weistrop, D. 2000, *ApJ*, 528, 260
- Konigl, A. & Kartje, J.F. 1994, *ApJ*, 434,446
- Kraemer, S.B. & Crenshaw, D.M. 2000, *ApJ*, submitted

- Kraemer, S.B., Crenshaw, D.M., Hutchings, J.B., Gull, T.R., Kaiser, M.E., Nelson, C.H.,  
& Weistrop, D. 2000, ApJ, 531, 278
- Nelson, C.H., Weistrop, D., Hutchings, J.B., Crenshaw, D.M., Gull, T.R., Kaiser, M.E.,  
Kraemer, S.B., & Lindler, D. 2000, ApJ, 531, 257
- Pedlar, A., Howley, P, Axon, D.J., & Unger, S.W. 1992, MNRAS, 259, 369
- Pérez-Fournon, I. & Wilson, A.S. 1990, ApJ, 356, 456
- Pier, E.A., et al. 1994, ApJ, 428, 124
- Reynolds, C.S. 1997, MNRAS, 286, 513
- Schulz, H. 1990, AJ, 99, 1442
- Schmitt, H.R. & Kinney, A.L. 1996, ApJ, 463, 498
- Weymann. R.J., Morris, S.L., Gray, M.E., & Hutchings, J.B. 1997, ApJ, 483, 717
- Winge, C., Axon, D.J., Macchetto, F.D., & Capetti, A. 1997, ApJ, 497, L121
- Winge, C., Axon, D.J., Macchetto, F.D., Capetti, A., & Marconi, A. 1999, ApJ, 519, 134

Fig. 1.— Comparison of radial velocities from STIS slitless spectra of the [O III] emission in NGC 4151, obtained at two different roll angles by Hutchings et al. (1998) and Kaiser et al. (2000).

Fig. 2.— Measurements of the [O III]  $\lambda 5007$  emission from STIS long-slit low-dispersion spectra, along the position angle  $221^\circ$  (see Nelson et al. 2000). Radial velocities are given relative to the systemic velocity from H I observations ( $997 \text{ km s}^{-1}$ ). Fluxes are in units of  $\text{ergs s}^{-1} \text{ cm}^{-2}$  for each  $0''.05 \times 0''.2$  bin.

Fig. 3.— Same as for Figure 2, except for a slit at position angle  $70^\circ$ , offset  $0''.1$  south of the nucleus.

Fig. 4.— Comparison of radial velocities from STIS long-slit observations of the [O III]  $\lambda 5007$  emission with those obtained from bright emission-line knots in the slitless spectra of Kaiser et al. (2000) that lie along the two slit positions.

Fig. 5.— Two-dimensional radial velocity maps for the outer surface of the biconical outflow model of NGC 4151, as they would appear on the sky: front side (left image) and back side (right image). The projected kinematic axis is vertical (corresponding to a position angle of  $60^\circ$  in the observations, NE at the top), and the relative positions of the  $0''.1$ -wide slits are shown in the near-side image. Deep purple, green, and dark red represent  $-700$ , zero, and  $+700 \text{ km sec}^{-1}$ , respectively.

Fig. 6.— Two-dimensional radial velocity maps for the outer surface of the biconical outflow model of NGC 1068, as they would appear on the sky: front side (left image) and back side (right image). The projected kinematic axis is vertical (corresponding to a position angle of  $15^\circ$  in the observations, NE at the top), and the relative position of the  $0''.1$ -wide slit is shown in the near-side image. Deep purple, green, and dark red represent  $-900$ , zero, and  $+900 \text{ km sec}^{-1}$ , respectively (see CK2000 for a comparison with the observations).

Fig. 7.— Comparison of model and observed radial velocities from the two long-slit positions. Errors in the observed radial velocities are smaller than the symbols, except as noted. The shaded regions are the envelopes of predicted radial velocities extracted from the slit positions in Figure 5.

Fig. 8.— Two dimensional distribution of radial velocities from the slitless spectra, with the vertical direction corresponding to the kinematic axis (at  $PA = 60^\circ$ ). The size of the symbol represents the magnitude of the radial velocity: “+” represents blueshifts and “x” represents redshifts, relative to the systemic velocity. The upper plot shows the observed values, and the lower plot shows the residuals (observed - model).

Fig. 9.— Comparison of model and observed radial velocities from the slitless observations (Kaiser et al. 2000).

Table 1. Kinematic Model of NGC 4151 (and NGC 1068)

Parameter	NGC 4151	NGC 1068
$z_{max}$	288 pc	306 pc
$\theta_{inner}$	20°	26°
$\theta_{outer}$	36°	40°
$i_{axis}$	40° (SW is closer)	5° (NE is closer)
$v_{max}$	750 km s <sup>-1</sup>	1300 km s <sup>-1</sup>
$r_t$	162 pc	137 pc

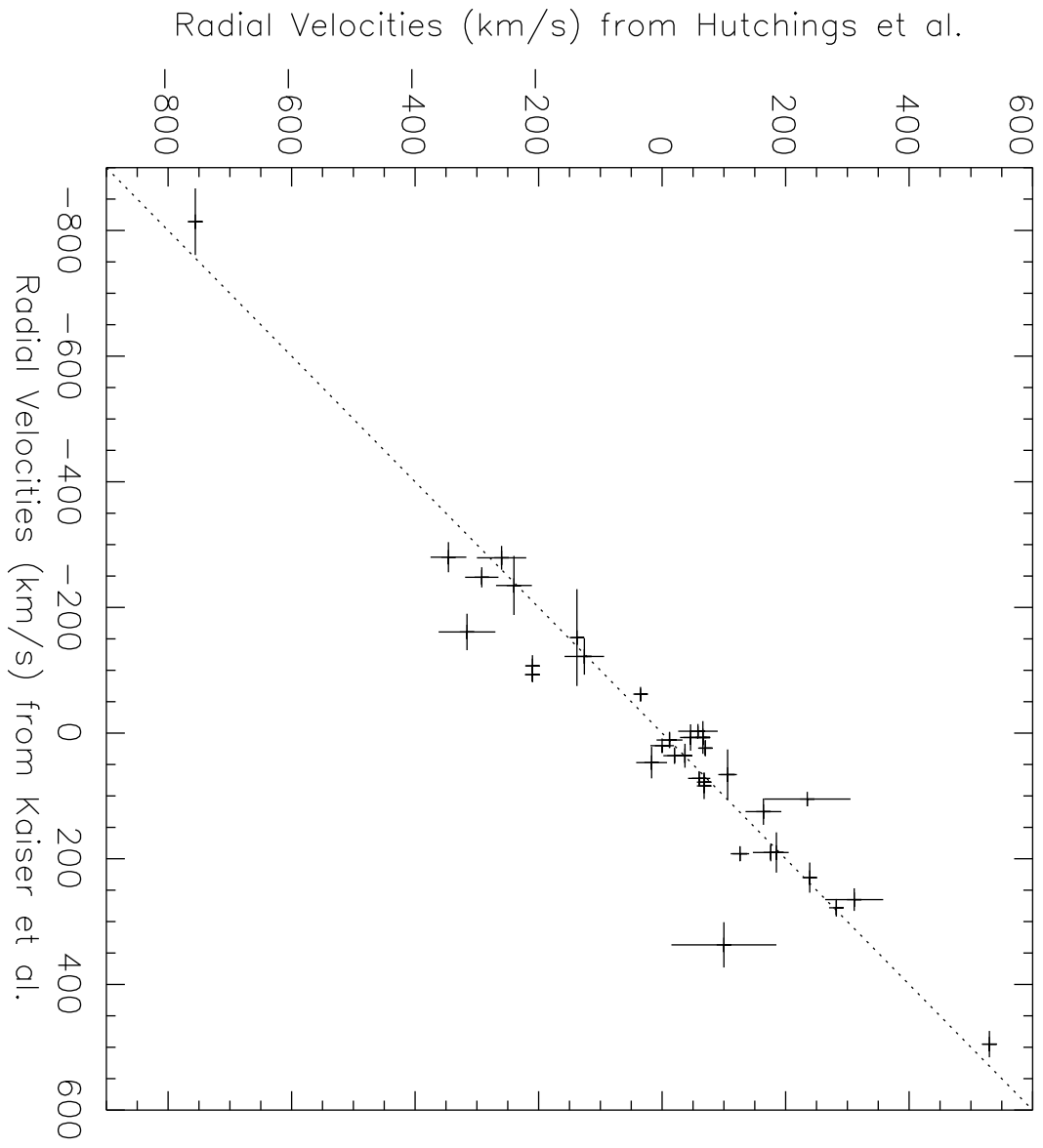


Fig. 1.

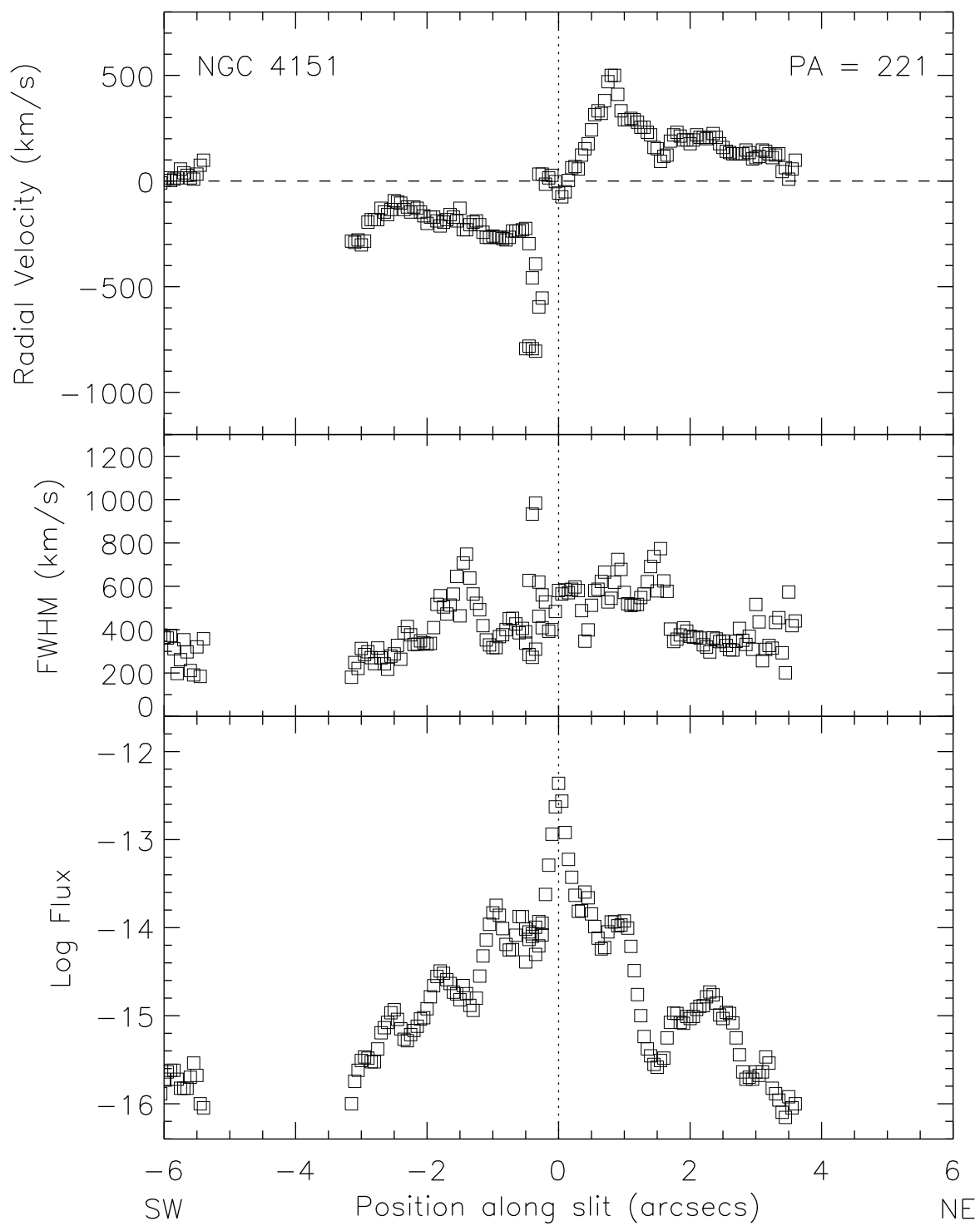


Fig. 2.

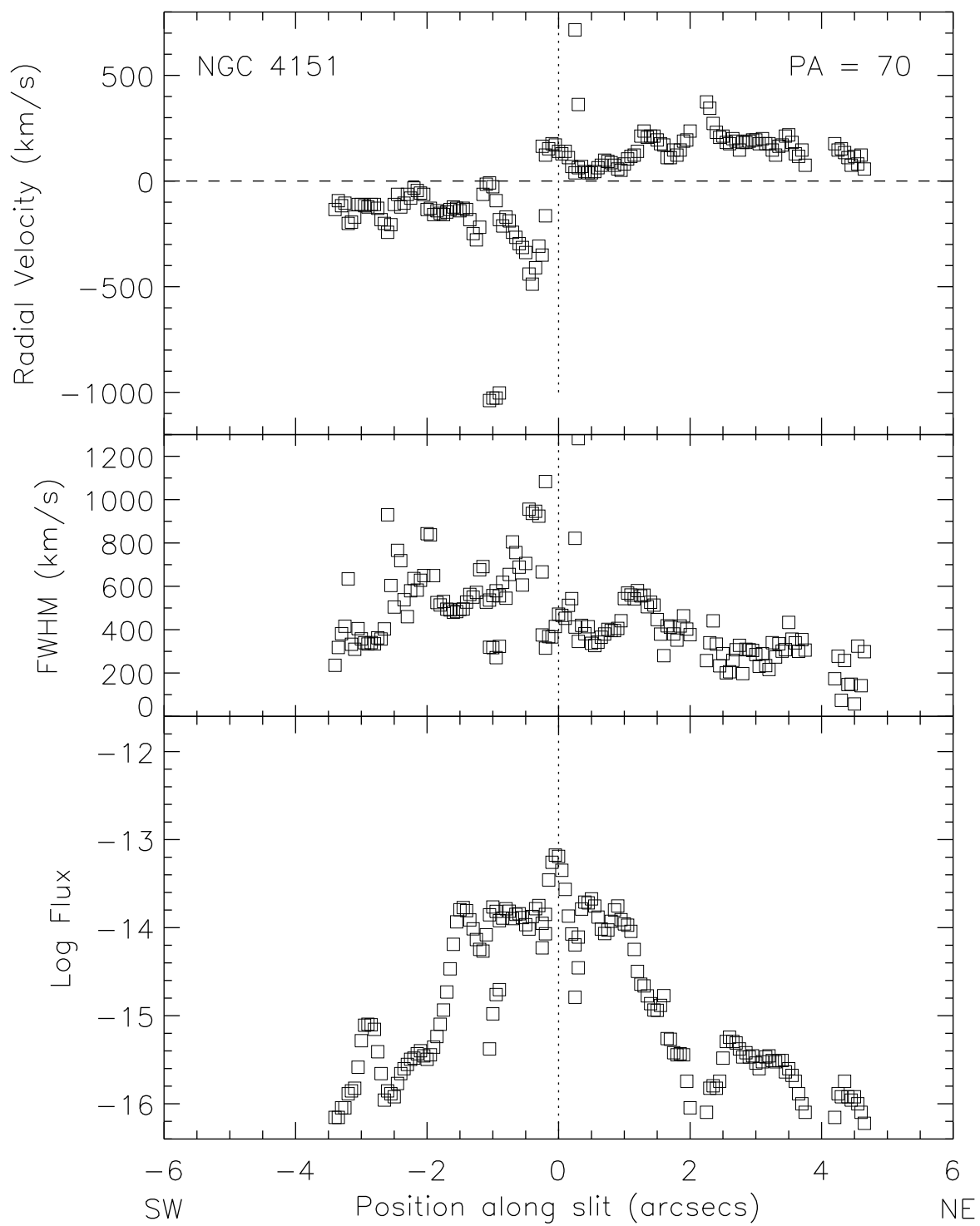


Fig. 3.

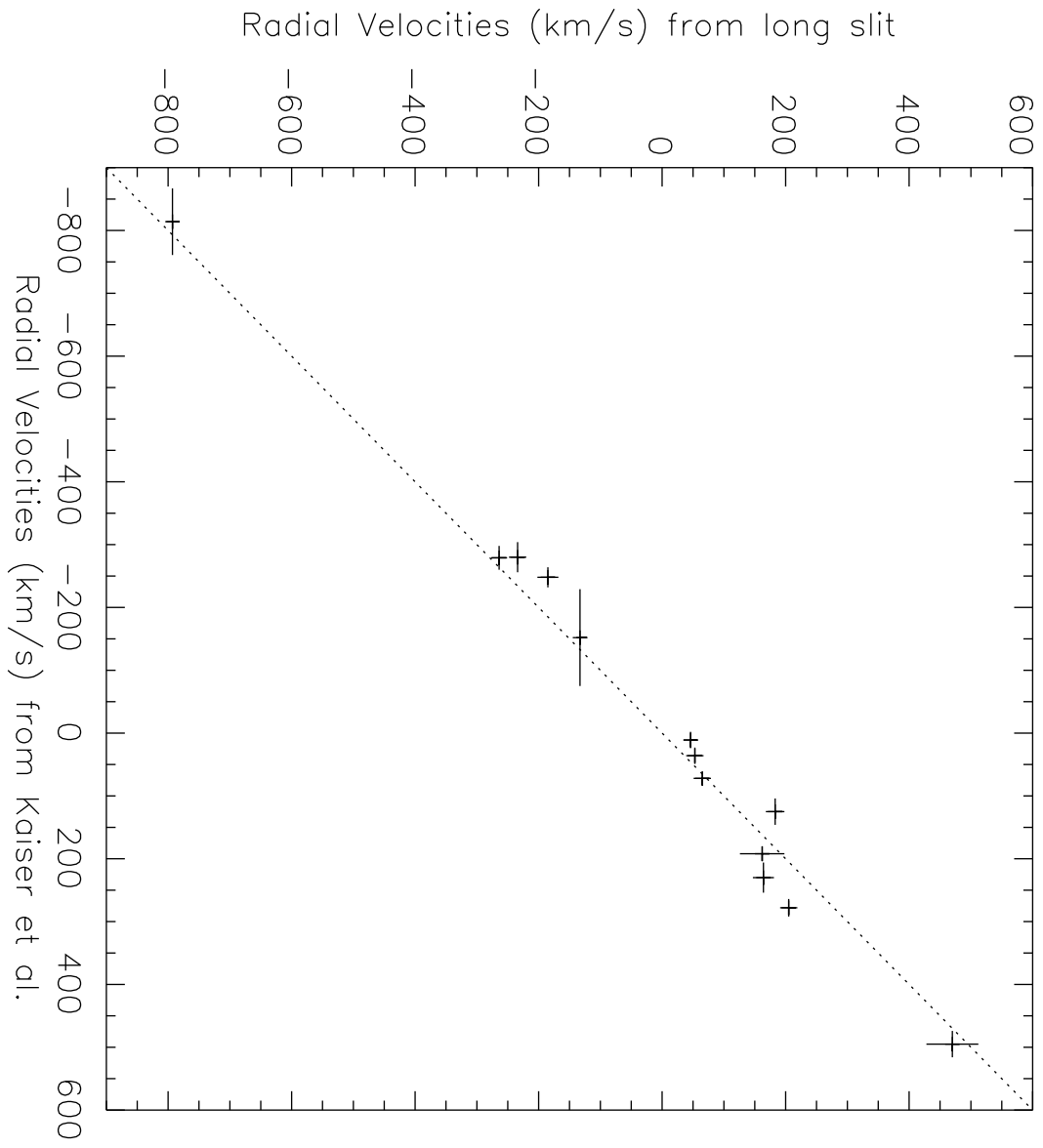


Fig. 4.

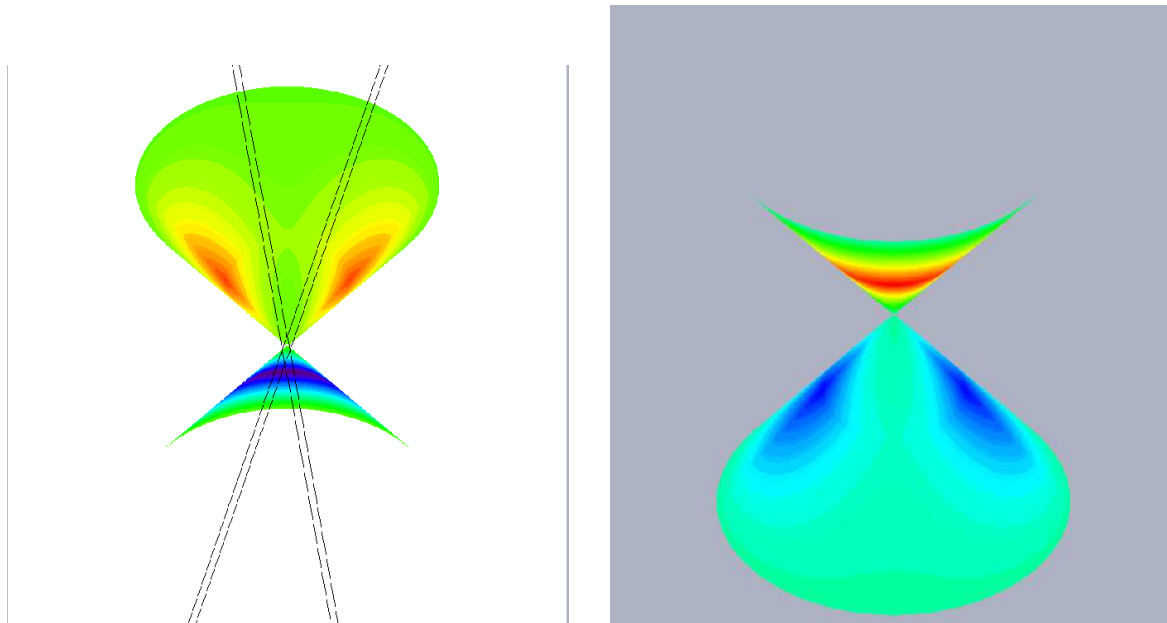


Fig. 5.

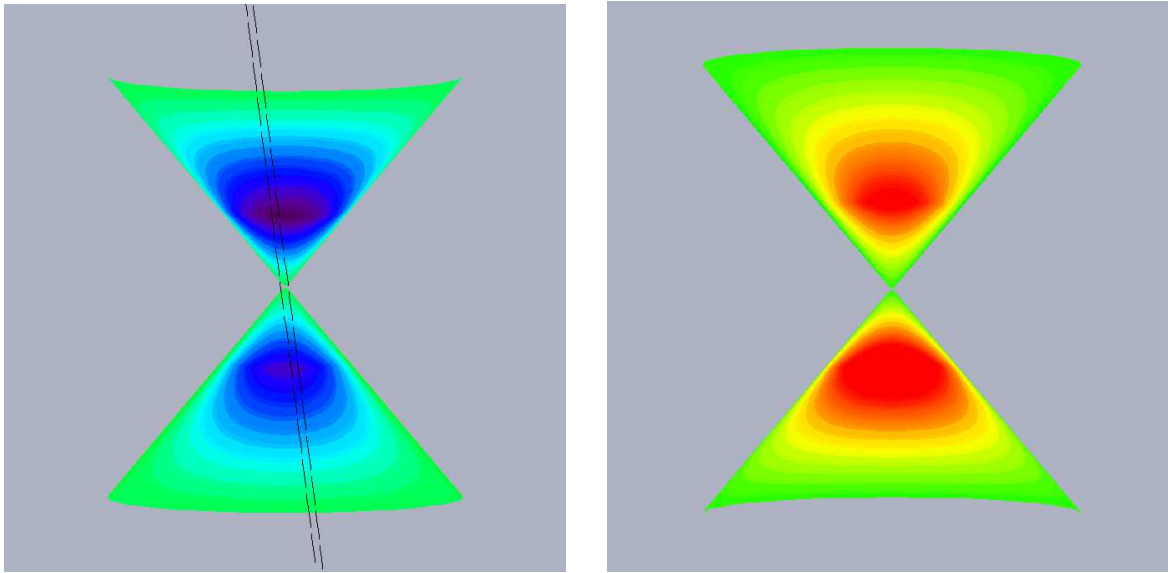


Fig. 6.

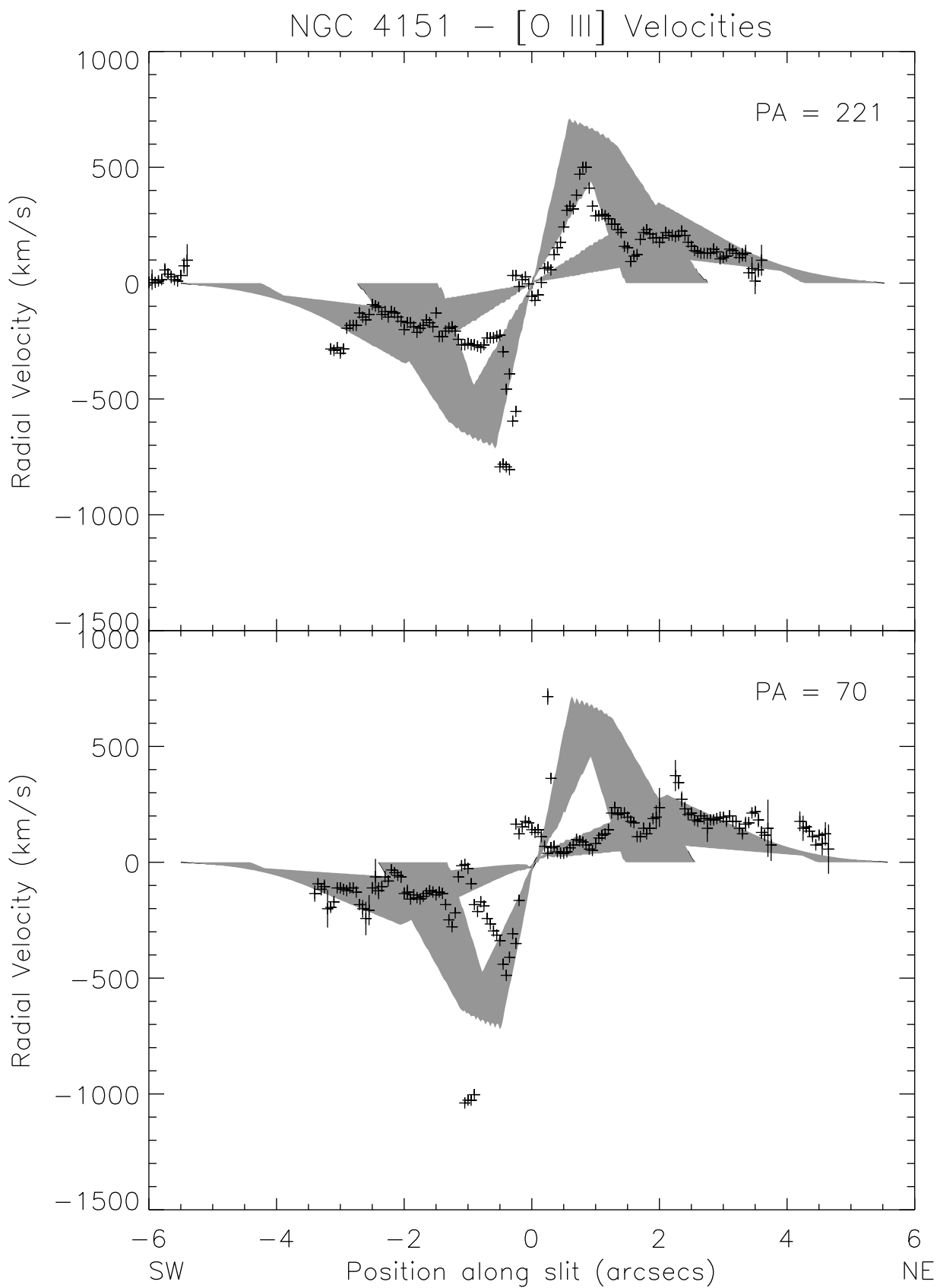


Fig. 7.

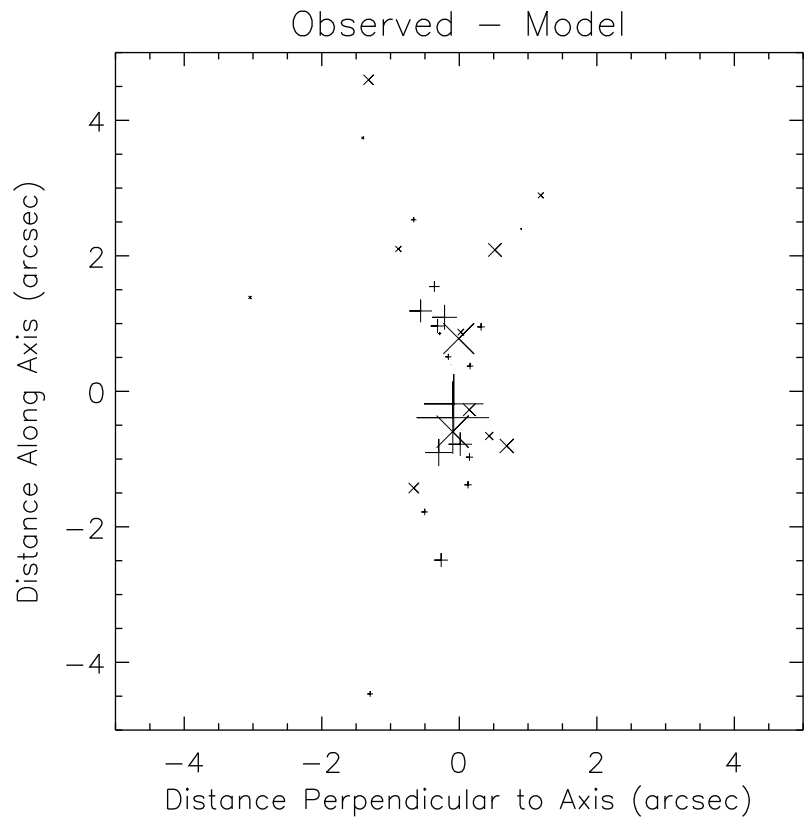
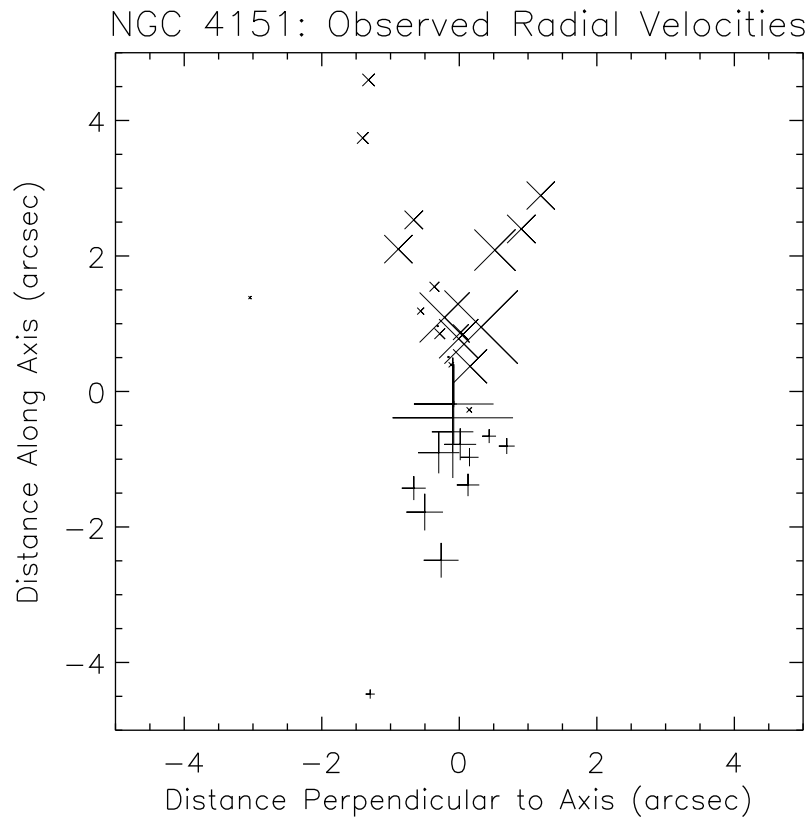


Fig. 8.

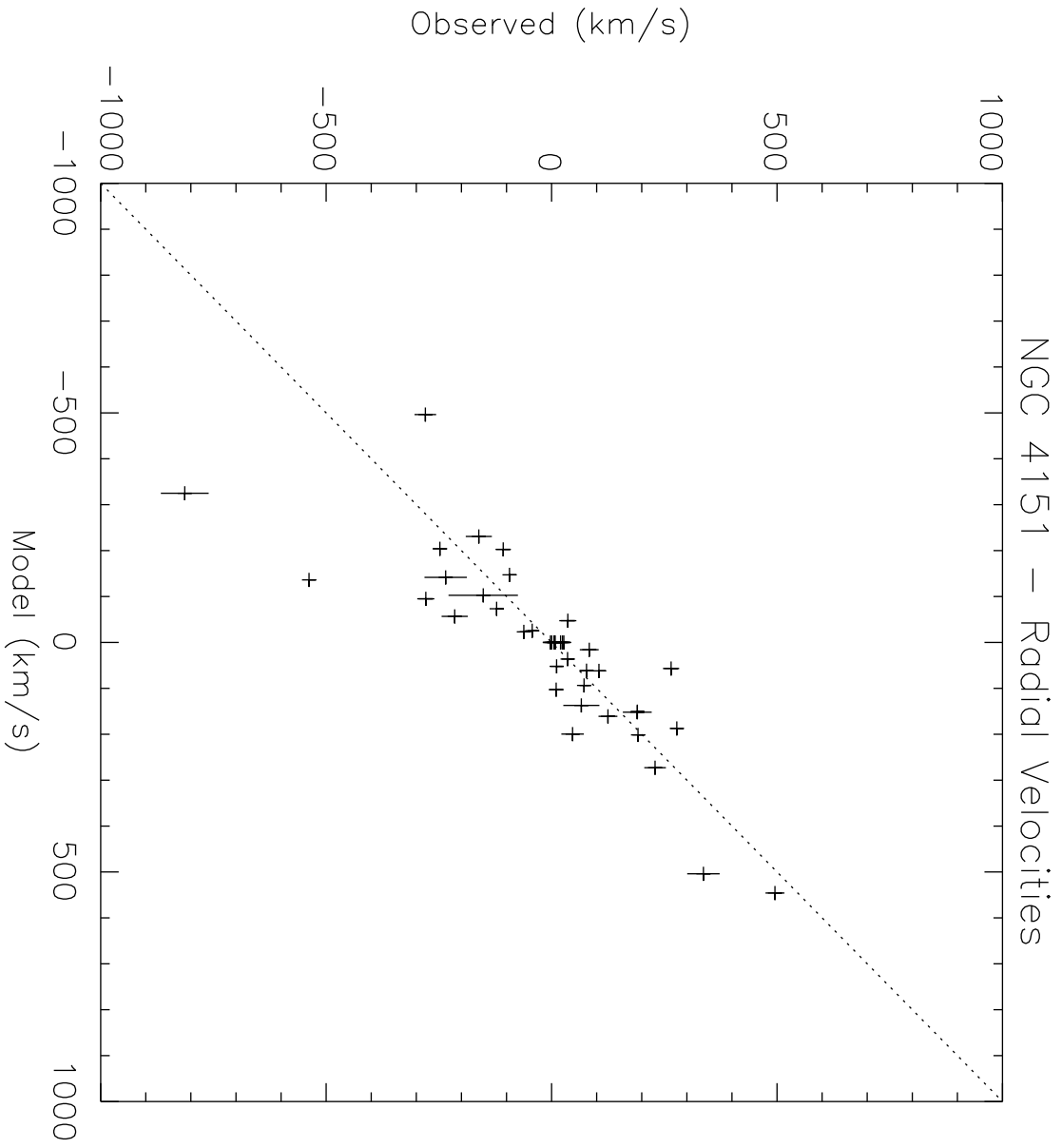


Fig. 9.